Atmos. Meas. Tech. Discuss., doi:10.5194/amt-2016-275, 2016
Manuscript under review for journal Atmos. Meas. Tech.
Published: 31 August 2016

Atmospheric Measurement Techniques
Open Access
Discussions

Field-of-view characteristics and resolution matching for the Global Precipitation Measurement (GPM) Microwave Imager (GMI)

Grant W. Petty[1] and Ralf Bennartz[2]

[1]Atmospheric and Oceanic Sciences, University of Wisconsin–Madison, 1225 W. Dayton St., Madison, WI, 53706, USA
[2]Earth and Environmental Sciences, Vanderbilt University, 5726 Stevenson Center, Nashville, TN 37240, USA

Correspondence to: Grant W. Petty (gwpetty@wisc.edu)

Abstract.

Representative parameters of the scan geometry are empirically determined for the Global Precipitation Measurement (GPM) Microwave Imager (GMI). Effective fields-of-view (EFOVs) are computed for the GMI's 13 channels taking into account the blurring effect of the measurement interval on the instantaneous fields-of-view (IFOVs). Using a Backus-Gilbert procedure, coefficients are derived that yield an approximate spatial match between synthetic EFOVs of different channels, using the 18.7 GHz channels as a target and with due consideration of the tradeoff between the quality of the fit and noise amplification and edge effects. Modest improvement in resolution is achieved in for the 10.65 GHz channels, albeit with slight "ringing" in the vicinity of coastlines and other sharp brightness temperature gradients. For all other channels, resolution is coarsened to approximate the 18.7 EFOV.

1 Introduction

Satellite passive microwave imagers have been playing a major role in the monitoring of the atmosphere and ocean and land surfaces since the 1970s. The most recent of these, launched 27 February 2014, is carried by the Global Precipitation Measurement (GPM) Core Observatory and is known as the GPM Microwave Imager (GMI; Hou et al. 2014).

The GMI has 13 channels ranging from 10.65 to 183 GHz, most with dual polarization (Table 1). As is true for most satellite passive microwave radiometers, the angular resolution of each channel is diffraction-limited, implying an instantaneous beamwidth – defined by the half-power (-3 dB) points on the antenna pattern – that is roughly proportional to $1/(\nu D_A)$, where ν is the channel frequency and D_A is the antenna diameter. The instantaneous field-of-view (IFOV) represents the projection of the angular antenna pattern onto the Earth's surface from the satellite's altitude and with incidence angle θ relative to the local normal. Because of practical limits on antenna sizes, microwave radiometers in space invariably have relatively coarse-resolution IFOVs at low frequencies (approximately 19×32 km at 10.65 GHz for the GMI) and progressively higher-resolution IFOVs with increasing frequency (about 4×6 km at 183 GHz).

Additional blurring is occasioned by the relative motion of the IFOV across the surface during the integration time Δt associated with each image pixel, giving rise to the effective field-of-view (EFOV), which is slightly larger than the IFOV in the direction of that relative motion.

The variable EFOV resolution implies that a pixel centered just offshore of a land mass could yield an 89 GHz measurement that is completely over ocean while yielding a 10.65 GHz observation that includes nearly equal proportions of land and ocean. This resolution mismatch between channels and the resulting inconsistency in scene properties can impair the ability of some geophysical retrieval algorithms to produce useful estimates in the presence of sub-FOV spatial variability.

Our objective here is to describe the performance of a resolution-matching algorithm applied to the nine GMI channels spanning 10.65 through 89 GHz. Specifically, we aim to bring all of these channels as close as possible to replicating the native EFOV of the 18.7 GHz channels. We do not attempt resolution-matching for the highest frequency channels (166 GHz and higher), because these are separately scanned in a way that does not preserve a fixed geometric relationship with the lower-frequency channels; thus, a fixed set of averaging coefficients is not possible.

As a byproduct of this work, we tabulate the previously unreported EFOV resolutions for all GMI channels, and we report a concise, self-consistent set of fixed parameters that collectively describe, to a reasonable approximation, the observed post-launch scan geometry of the GMI. While these are no substitute for the detailed ephemeris and navigation data provided with the imagery for each orbit, they may be useful for the realistic simulation of GMI images from atmospheric and terrestrial models.

2 Native Sensor Characteristics

2.1 Overview

The GMI is a conically scanning radiometer whose antenna beam maintains an approximately constant incidence angle with respect to the Earth's surface as it rotates about the vertical axis that connects the satellite with the satellite's subpoint (Fig. 1). The parameters of importance include a) the relative speed of the satellite subpoint across the Earth's surface, which is determined by the orbital period and, to a far lesser degree, by the Earth's own rotation, b) the rotation rate of the antenna, c) the incidence angle of the antenna beam and thus the angular radius of the scan, d) the integration time Δt, which determines the both the along-scan separation between pixels and also the smearing effect that expands the EFOV relative to the IFOV, and e) the total number of sampled pixels along one scan. The latter is in turn tied to the fraction of one complete circular scan that is actually sampled and thus also to the total swath width.

Note that there are two different sets of feed horns associated with the 10.65–89 GHz channels (channels 1–9) and with the 166 and 183.3 GHz channels (10-13), respectively. The latter channels view the Earth at a slightly steeper angle. Consequently, their data swath is narrower, and their scan pattern is spatially misregistered with that of the lower frequency channels, as shown in Fig. 2. Finally, because of the oblateness of the Earth, the relative registration in the along-track direction fluctuates by up to several tenths of the spacing between scan lines.

Atmos. Meas. Tech. Discuss., doi:10.5194/amt-2016-275, 2016
Manuscript under review for journal Atmos. Meas. Tech.
Published: 31 August 2016

2.2 Scan geometry model

The geometry of the GMI scans must be accurately modeled both to compute the actual EFOV sizes and shapes and to compute the overlap between adjacent EFOVs. Both are required in order to be able to determine the correct weights for constructing synthetic (resolution-matched) FOVs for each channel.

Here we model the orbit of the GMI as circular with fixed altitude above the Earth's surface and fixed period, and we ignore the oblateness of the Earth. By carefully examining actual post-launch GMI data, a set of geometrically self-consistent values for all major parameters of the scan geometry were either directly measured or inferred. These values are reported in Table 2.

Note that we ignore the variable correction due to the Earth's own rotation, but we introduce a small constant correction to the subtrack velocity relative to that predicted from the orbital velocity at the given altitude. Thus, our model can be thought of as approximating the mean scan geometry of the GMI while being subject to minor fluctuating errors that are negligible for nearly contiguous pixels but larger for widely separated pixels.

2.3 EFOV properties

The effective field-of-view (EFOV) of each GMI channel results from convolving the instantaneous field-of view (IFOV), or the antenna gain pattern projected onto the Earth's surface, with the spatial displacement due to scanning and to satellite motion during the integration time. The IFOV is currently modeled as Gaussian, as measured sidelobe gains are at least 30 dB below that of the main beam for all channels and are negligible for the present purpose. The computed EFOV dimensions are reported in Table 1, and a schematic depiction of the change in EFOV resolution relative to the IFOV is shown in Fig. 3. Because the smearing effect of the time integration is almost entirely in the along-scan direction, only that dimension is measurably changed for the EFOV relative to the IFOV. It is most pronounced for the highest resolution IFOVs.

Note also that the interscan distance of 13.15 km is significantly larger than the cross-scan EFOV dimension of 7.2 km for the 89.00 GHz channels. In other words, these channels provide non-contiguous coverage. That in turn implies that no spatial average of 89 GHz EFOVS can closely approximate the EFOV of any lower-frequency channel.

3 FOV-Matching Methodology

3.1 Overview

To address the large mismatch in EFOV sizes between lower and higher frequency channels, we have two choices. We can

– spatially average (convolve) higher resolution channels to approximately match the coarser resolution of a lower-frequency channel; or

– sharpen (deconvolve) the lowest resolution channel(s) to approximate a higher frequency channel's EFOV.

In both cases, resolution-matching requires one to linearly combine the observations from a set of contiguous pixels so as to approximate the desired target EFOV. The new (synthetic) EFOV is simply the weighted sum of the original EFOVs. To

Atmos. Meas. Tech. Discuss., doi:10.5194/amt-2016-275, 2016
Manuscript under review for journal Atmos. Meas. Tech.
Published: 31 August 2016

Atmospheric Measurement Techniques Discussions

achieve resolution sharpening, there must be both positive and negative weights, but they must all sum to unity to conserve the total radiance in the image.

It must be emphasized that it is generally not possible to achieve a perfect match. One can only aim to achieve the *best possible* match and then examine the empirical quality of the outcome. This is especially true in the case of deconvolution, as weighting coefficients must be determined so as to achieve reasonable improvements in resolution without unwanted artifacts such as excessive noise amplification and/or "ringing." Also, deconvolution is only possible when the pixel spacing is significantly smaller than the size of the EFOV whose resolution one is seeking to improve. As a practical matter, this limits the use of deconvolution for the GMI to the 10.65 GHz channels. Finally, the ability to match FOVs is degraded right at the edge of the swath.

Our efforts here are similar to those reported for earlier microwave imagers, such as the the Special Sensor Microwave Imager (Farrar and Smith, 1992; Robinson et al., 1992), the TRMM Microwave Imager (Bauer and Bennartz, 1998), the Advanced Microwave Sounding Unit (Bennartz, 2000), and the Advance Scanning Microwave Radiometer for the Earth Observing System (Wang et al., 2011). Apart from Bennartz (2000) and Wang et al. (2011), most of these do not examine the actual properties of the resulting synthetic EFOVs.

3.2 Coefficient determination

In the classic method of Backus and Gilbert (1968, 1970), which was in turn adapted to satellite passive microwave images by Stogryn (1978), a cost function is defined that incorporates both a measure of noise amplification and a quadratic measure of resolution or "spread." A tuning parameter γ allows the relative emphasis on each of the two terms to be varied. Our own method is essentially the Backus-Gilbert method, but we replace the second term ("spread") with one representing spatial correlation between the synthetic FOV (constructed from a linear sum of overlapping real EFOVs) and the target EFOV, in this case the native EFOV of the 18.7 GHz channels. Thus, for the 10.65 GHz channels, our procedure attempts to sharpen the resolution within the limits of spatial sampling and noise amplication considerations. For the higher frequency channels, the procedure leads to a spatial averaging.

Farrar and Smith (1992) take a similar approach to ours in their deconvolution of SSM/I brightness temperatures, except that their target EFOV was an idealized uniform disk with sharp edges rather than a real (and therefore smooth) EFOV. Otherwise the mathematics is the same.

Fundamentally, the method entails taking a linear sum of multiple FOVs overlapping the target FOV. That is, if the target FOV is denoted $F_0(x,y)$, then our goal is to create a synthetic FOV $F'(x,y)$ for another channel such that

$$F_0(x,y) \approx F'(x,y) = \sum_i w_i f_i(x,y), \tag{1}$$

where w_i are appropriately chosen linear weights applied to each of the original FOVs (or pixels) f_i in the neighborhood of F_0. Note that to conserve brightness temperature, the weights must sum to unity:

$$\sum_i w_i = 1. \tag{2}$$

Atmos. Meas. Tech. Discuss., doi:10.5194/amt-2016-275, 2016
Manuscript under review for journal Atmos. Meas. Tech.
Published: 31 August 2016

Atmospheric Measurement Techniques Discussions

The quality of F' as an approximation to F_0 can be defined in various ways. Here, we choose the squared deviation integrated over area:

$$\chi^2 = \iint \left[F'(x,y) - F_0(x,y)\right]^2 \, \mathrm{d}x \, \mathrm{d}y \tag{3}$$

If the channel being operated on has a higher frequency than the reference channel, then its native resolution is generally higher than that of the reference channel. FOV matching then reduces to a spatial averaging or blurring procedure, and most or all of the coefficients in (1) are positive. If, on the other hand, coarser resolution FOVs are being combined in an effort to match a finer-resolution target FOV, then this amounts to a deconvolution, or sharpening procedure, and the weights will necessarily be both positive and negative as needed to cancel the response outside the target FOV.

A well-known problem with deconvolution, when not done carefully, is that the individual magnitudes of w_i can become quite large (while still satisfying Eq. 2), leading to severe noise amplification as well as "ringing" in the deconvolved image in the presence of sharp brightness temperature gradients. The measure of the noise variance amplification associated with a linear filter is

$$N^2 = \sum_i w_i^2, \tag{4}$$

since the effective noise variance in the processed image is then

$$\sigma^2_{\mathrm{post}} = N^2 \sigma^2_{\mathrm{pre}}, \tag{5}$$

where σ^2_{pre} is the "native" noise present in the original image, including possibly geophysical noise and/or uncertainties in the precise FOV shape in addition to instrument noise.

Given (2), N^2 is absolutely minimized when the w_i are all positive and equal, corresponding to a pure averaging or blurring procedure. On the other hand, N^2 can become arbitrarily large when pushing the limits of a deconvolution or sharpening procedure. In any case, whether sharpening or blurring the image, it is important to consider the inevitable tradeoff between achieving the best possible fit to the target FOV and controlling noise amplification and ringing.

Even apart from noise amplification considerations, it is generally impossible to exactly match an arbitrary target FOV via a sum over the discrete set of neighboring FOVs of different size and shape. This is especially true when the pixel density (spatial sampling) is poor relative to the resolution of the target FOV. The target FOV is therefore indeed *only* a target and is never actually achieved in the footprint matching procedure. Rather, one must examine the resulting synthetic FOV F' to determine how good the fit actually is and whether the procedure is of sufficient utility to be worth the effort.

For convenient reference, we provide the full derivation in Appendix A.

3.3 Noise vs. fit

Figure 4 depicts the tradeoffs between noise factor and fit to the target EFOV. For 10.65 GHz, we did not want to exceed a noise amplification factor of about 2, which limited the quality of the fit to the target EFOV defined by the 18.70 GHz channels. Even without this constraint, the fit could only be improved by a few percent. For 23.80 and 36.50 GHz, an excellent fit approaching

100% is achievable for all but the edge pixels without any noise amplification. For 89.00, a relatively poor fit is achieved owing to significant undersampling by the native FOVs in the cross-scan direction. Overall, we find that a constant tuning value of $\gamma = 6 \times 10^{-6}$ yields a reasonable compromise between fit and noise amplification for all channels.

4 Results

4.1 Synthetic EFOVs

Figure 5 depicts the shapes of the final synthetic EFOVs for pixel 110 (center of the swath). Of particular note are the following points: While there is modest improvement in the 10.65 GHz fit to the target 18.70 GHz EFOV, it is not possible to actually match that resolution. As found previously by Bauer and Bennartz (1998) for the TRMM Microwave Imager, the improvement is better in the along-scan direction due to more oversampling in that direction. There are significant negative sidelobes in the synthetic EFOVs for 10.65 GHz. This appears to be unavoidable given the available sampling for these channels. The fit for 23.80 and 36.5 GHz is excellent.

Because the 89.00 GHz channels are badly undersampled in the cross-scan direction, the synthetic FOV fit to the target EFOV is poor in that direction. It is quite good in the along-scan direction. All of the above results are worst-case for the entire interior of the data swath, as the sampling density improves toward the edges. At the edges, however, the fit will deteriorate again. Table 3 gives the half-power beamwidths of the synthetic EFOVs compared to the native resolution for each channel. (Note that the half-power value does not give a useful measure of the improvement in the fit for 89.00 GHz, owing to the multimodal shape.)

4.2 Application to real data

Figure 6 depicts the implications of various values of γ for the deconvolution of actual 10.65 GHz imagery. To make the differences most visible, a swath segment was chosen that includes numerous islands as well was some cellular convection. As one progresses to greater sharpening, “overshoot” (Gibbs effect) becomes evident in the vicinity of sharp gradients. Based on our analysis, this appears to be an unavoidable artifact of any significant sharpening of the 10.65 GHz resolution, given the less-than-ideal spatial sampling.

For the chosen value of $\gamma = 6 \times 10^{-6}$, Fig. 7 depicts a sample of real GMI data with (right column) and without (left column) the (de)convolution procedure applied. Improved consistency in apparent resolution between channels is apparent in the right column, as expected.

5 Conclusions

This paper documents the effective fields-of-view (EFOVs) of the GMI after allowing for the blurring effect of the measurement interval on the instantaneous fields-of-view (IFOVs). We derived coefficients that produce an approximate spatial match

Atmos. Meas. Tech. Discuss., doi:10.5194/amt-2016-275, 2016
Manuscript under review for journal Atmos. Meas. Tech.
Published: 31 August 2016

between synthetic EFOVs of different channels, using the 18.7 GHz channels as a target and with reasonable tradeoffs between the quality of the fit and noise amplification.

No set of coefficients is capable of generating an ideal matching between the 10.65 GHz channels and the target EFOV, because they are not sufficiently densely sampled. However, there is modest improvement in resolution, albeit with slight "ringing" in the vicinity of coastlines and other sharp brightness temperature gradients. Depending on the application, one must decide whether the introduced artifacts or the improved resolution is of greater importance.

At 89 GHz, the averaging to coarser resolution does not yield a good fit to the 18.7 EFOV, because the spacing between 89 GHz scans is too large relative to the cross-scan pixel resolution. Nevertheless, the average is still a significantly better match to the 18.7 GHz EFOV than the unconvolved imagery.

For all other channels, the matching procedure yields an excellent fit. Resolution matching coefficients are available from the corresponding author upon request.

Appendix A: Derivation

Our goal is to find the set of weights w_i satisfying (2) that also minimize the cost function

$$\Phi = \gamma N^2 + \chi^2, \tag{A1}$$

where γ is a tunable parameter that controls relative importance of noise amplification vs. goodness-of-fit. Expanding, we have

$$\Phi = \gamma \sum_i w_i^2 + \iint \left[\sum_i w_i f_i(x,y) - F_0(x,y) \right]^2 \mathrm{d}x\, \mathrm{d}y. \tag{A2}$$

For notational simplicity, the explicit dependence of f_i and F_0 on (x,y) will suppressed in the equations that follow.

Expanding the squared term and taking constant terms outside of the integrals yields

$$\Phi = \gamma \sum_i w_i^2 + \sum_i w_i \sum_j w_j \iint f_i f_j \,\mathrm{d}x\,\mathrm{d}y - 2 \sum_i w_i \iint F_0 f_i \,\mathrm{d}x\,\mathrm{d}y + \iint F_0^2 \,\mathrm{d}x\,\mathrm{d}y. \tag{A3}$$

The integral terms are all constants, and we may make the following notational substitutions:

$$P_{ij} \equiv \iint f_i f_j \,\mathrm{d}x\,\mathrm{d}y \quad ; \quad q_i \equiv \iint F_0 f_i \,\mathrm{d}x\,\mathrm{d}y \quad ; \quad r \equiv \iint F_0^2 \,\mathrm{d}x\,\mathrm{d}y. \tag{A4}$$

Employing the Einstein convention of implied summation over pairs of like indices, our cost function can be written simply as

$$\Phi = \gamma w_i w_i + w_j P_{jk} w_k - 2 w_m q_m + r. \tag{A5}$$

We wish to find the coefficients w that minimize Φ subject to the constraint (2). The conventional method for solving a constrained optimization problem is the method of Lagrange multipliers. We define a new function

$$\Lambda = \gamma w_i w_i + w_j P_{jk} w_k - 2 w_m q_m + r + \lambda \left(\sum_n w_n - 1 \right), \tag{A6}$$

Atmos. Meas. Tech. Discuss., doi:10.5194/amt-2016-275, 2016
Manuscript under review for journal Atmos. Meas. Tech.
Published: 31 August 2016

where λ is the Lagrange multiplier, and the added term it multiplies is zero when the constraint is satisifed. The task is then to solve the set of equations corresponding to the combination of (2) with the results of

$$\frac{\partial}{\partial w_p}\Lambda = 0. \tag{A7}$$

Carrying out the above differentiation yields

$$\begin{aligned}\frac{\partial \Lambda}{\partial w_p} &= \frac{\partial}{\partial w_p}\left[\gamma w_i w_i + w_j P_{jk} w_k - 2 w_m q_m + r + \lambda\left(\sum_n w_n - 1\right)\right] \\ &= 2\gamma w_p + 2P_{pk}w_k - 2q_p - \lambda \\ &= 0\end{aligned}$$

Factoring out the 2 and expressing the last two lines above in matrix notation, we have

$$\mathbf{B}\mathbf{w} = \mathbf{q} + \frac{\lambda}{2}\mathbf{u}, \tag{A8}$$

where $\mathbf{u} = (1, 1, \cdots, 1)^{\mathsf{T}}$, and

$$B_{ij} = P_{ij} + \gamma\delta_{ij}, \tag{A9}$$

where δ_{ij} is the Kronecker delta. That is, the matrix $\mathbf{B}$ is just the matrix $\mathbf{P}$ with the tuning parameter γ added to each diagonal element.

The solution for the desired coefficients is then

$$\mathbf{w} = \mathbf{B}^{-1}\left[\mathbf{q} + \frac{\lambda}{2}\mathbf{u}\right], \tag{A10}$$

We still have the undetermined Lagrange multiplier λ. Its value follows from the constraint (2):

$$\begin{aligned}\sum_i w_i &= \sum_i \left(\mathbf{B}^{-1}\mathbf{q}\right)_i + \frac{\lambda}{2}\sum_i \left(\mathbf{B}^{-1}\mathbf{u}\right)_i \\ &= \mathbf{u}^{\mathsf{T}}\mathbf{B}^{-1}\mathbf{q} + \frac{\lambda}{2}\mathbf{u}^{\mathsf{T}}\mathbf{B}^{-1}\mathbf{u} \\ &= 1,\end{aligned}$$

leading to

$$\lambda = \frac{2\left(1 - \mathbf{u}^{\mathsf{T}}\mathbf{B}^{-1}\mathbf{q}\right)}{\mathbf{u}^{\mathsf{T}}\mathbf{B}^{-1}\mathbf{u}}. \tag{A11}$$

Note that the denominator is just the sum over all elements of $\mathbf{B}$.

Acknowledgements. This work was supported by NASA Grants NNX13AG49G and NNX16AF70G through the Precipitation Measurement Mission.

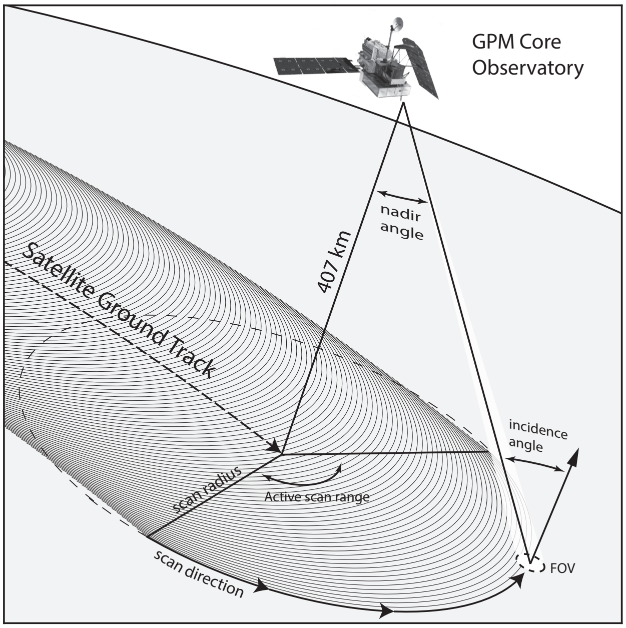

Figure 1. Schematic depiction of the scan geometry of the GMI. The dashed circle represents the instantantaneous intersection of the cone of constant incidence angle with the Earth's surface. Its radius and other characteristic parameters are given in Table 2.

.

References

Backus, G. and Gilbert, F.: The Resolving power of Gross Earth Data, Geophys. J. R. Astron. Soc., 16, 169–205, 1968.

Backus, G. and Gilbert, F.: Uniqueness in the Inversion of inaccurate Gross Earth Data, Philos. Trans. R. Soc. of London A, 266, 123–192, 1970.

Bauer, P. and Bennartz, R.: Tropical Rainfall Measuring Mission microwave imaging capabilities for the observation of rain clouds, Radio Sci., 33, 335–349, 1998.

Bennartz, R.: Optimal convolution of AMSU-B to AMSU-A, J. Atmos. Ocean Technol., 17, 1215–1225, 2000.

Farrar, M. and Smith, E.: Spatial resolution enhancement of terrestrial features using deconvolved SSM/I microwave brightness temperatures, IEEE Trans. Geosci. Remote Sens., 30, 349–355, 1992.

Hou, A. Y., Kakar, R. K., Neeck, S., Azarbarzin, A. A., Kummerow, C. D., Kojima, M., Oki, R., Nakamura, K., and Iguchi, T.: The Global Precipitation Measurement Mission, Bull. Amer. Met. Soc., 95, 701–722, doi:10.1175/BAMS-D-13-00164.1, http://dx.doi.org/10.1175/BAMS-D-13-00164.1, 2014.

Robinson, W., Kummerow, C., and Olson, W.: A technique for enhancing and matching the resolution of microwave measurements from the SSM/I instrument , IEEE Trans. Geosci. Rem. Sens., 30, 419–429, 1992.

Stogryn, A.: Estimates of brightness temperatures from scanning radiometer data, IEEE Trans. Antenna Propagat., AP-26, 720–726, 1978.

Wang, Y.-Q., Shi, J.-C., Jiang, L.-M., Du, J.-Y., and Tian, B.-S.: The development of an algorithm to enhance and match the resolution of satellite measurements from AMSR-E, Science China Earth Sciences, 54, 410–419, 2011.

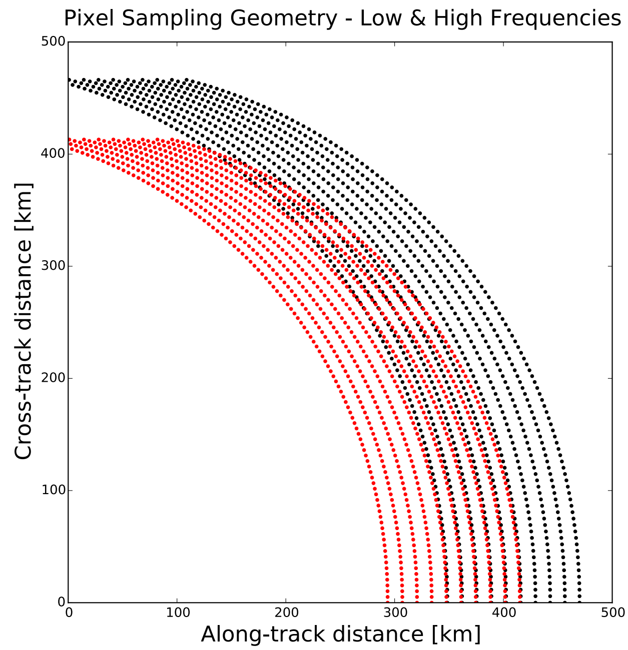

Figure 2. The modeled spatial relationship between pixel centers for 10.65–89 GHz (black) and 166–183.3 GHz (red). The horizontal axis gives along-track distance from an arbitrary starting point; the vertical axis gives cross-track distance measured from the satellite subtrack.

.

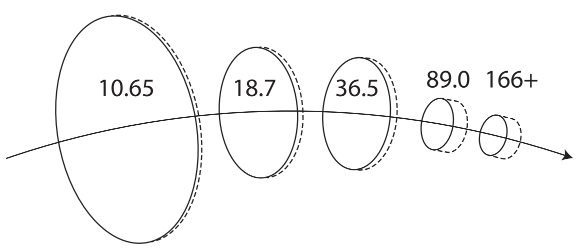

Figure 3. Schematic depiction of the difference between the instantaneous field-of-view (IFOV) and the effective field-of-view (EFOV) for different channels of the GMI, as measured at the half-power points of the effective antenna functions. The scan curvature is exaggerated.

.

Atmos. Meas. Tech. Discuss., doi:10.5194/amt-2016-275, 2016
Manuscript under review for journal Atmos. Meas. Tech.
Published: 31 August 2016

Atmospheric Measurement Techniques
Discussions

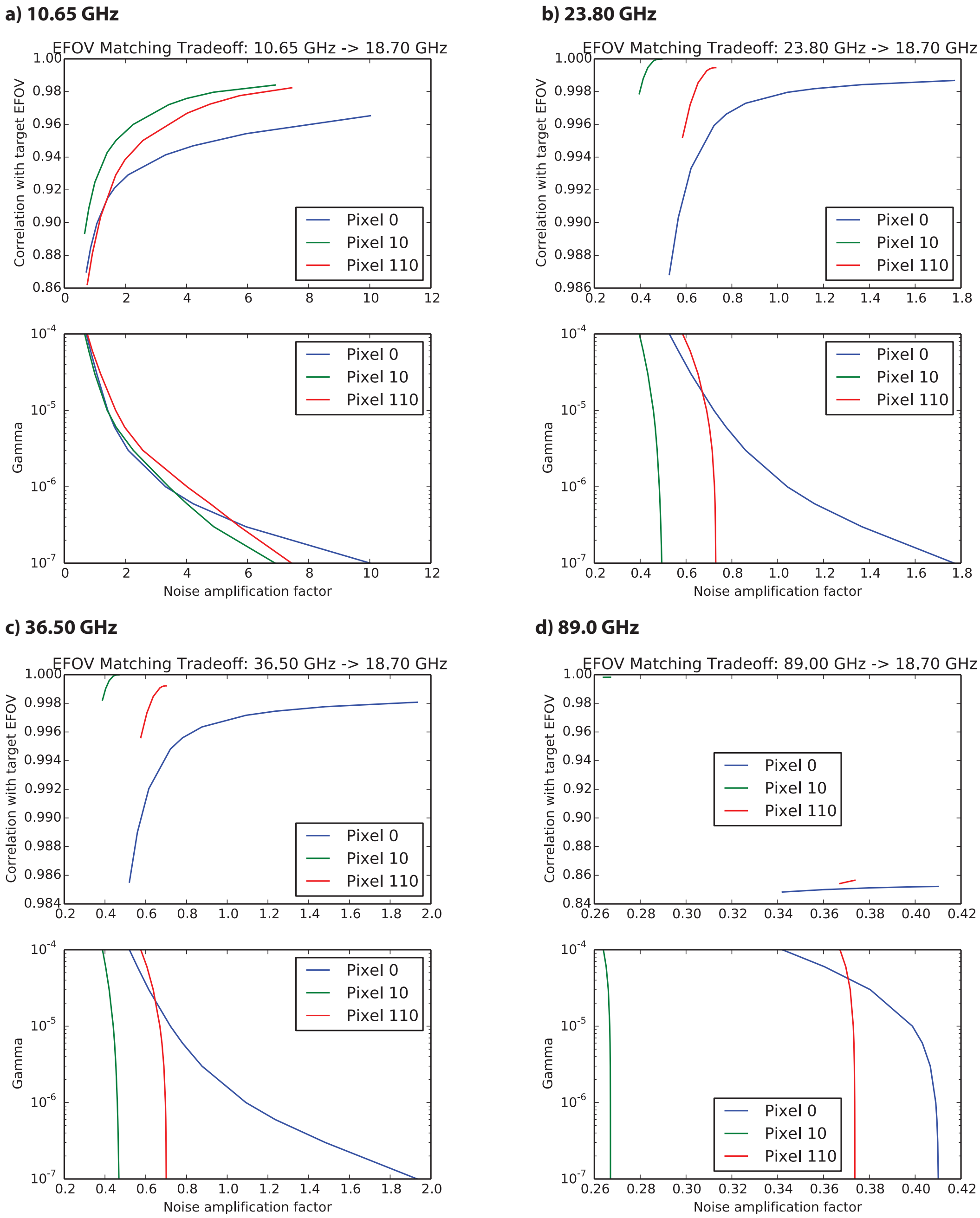

Figure 4. Relationship between noise factor, fit to the target EFOV, and the gamma parameter for the a) 10.65 GHz, b) 23.80 GHz, c) 36.5 GHz, and d) 89.0 GHz channels. For each frequency, the top panel depicts the tradeoff between the fit (as indicated by the spatial correlation coefficient) and the noise factor; the bottom panel depicts the relationship between the gamma parameter and the noise factor. Pixel 0 is the first pixel in the scan, where the possibility for EFOV matching is partially limited by the absence of overlapping pixels beyond the edge of the swath. Pixel 10 is an interior pixel with comparatively high spatial sampling density, allowing for the best fits. Pixel 110 is at the center of the swath, where the sampling density is least.

Atmos. Meas. Tech. Discuss., doi:10.5194/amt-2016-275, 2016
Manuscript under review for journal Atmos. Meas. Tech.
Published: 31 August 2016

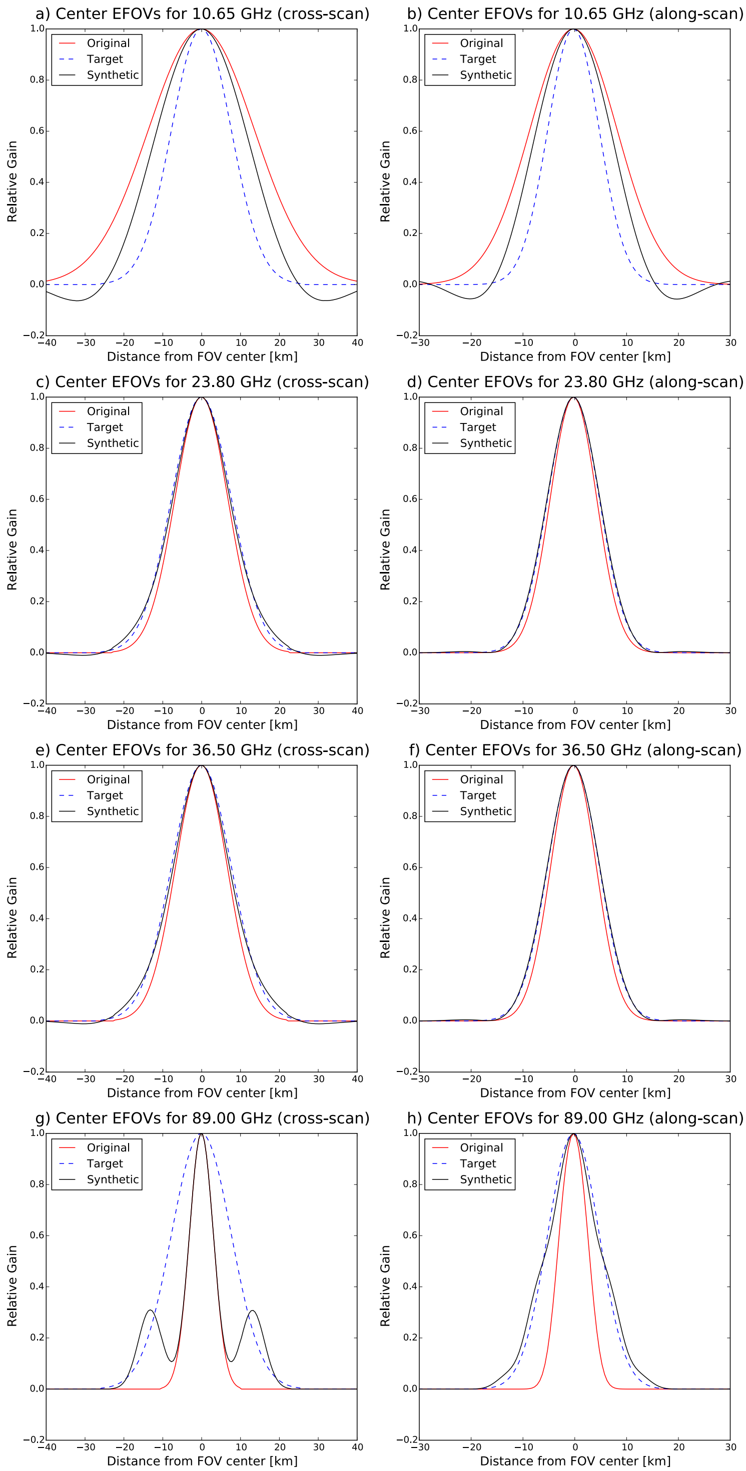

Figure 5. From top to bottom, the shape of the final synthetic EFOVs at the center of the swath for 10.65, 23.80, 36.5, and 89.0 GHz (solid curves). For comparison, the native EFOVs (red curve) and target 18.70 GHz EFOV (blue dashed curve) are shown. The left column is for the cross-scan direction; the right column is for the along-scan direction.

Atmos. Meas. Tech. Discuss., doi:10.5194/amt-2016-275, 2016
Manuscript under review for journal Atmos. Meas. Tech.
Published: 31 August 2016

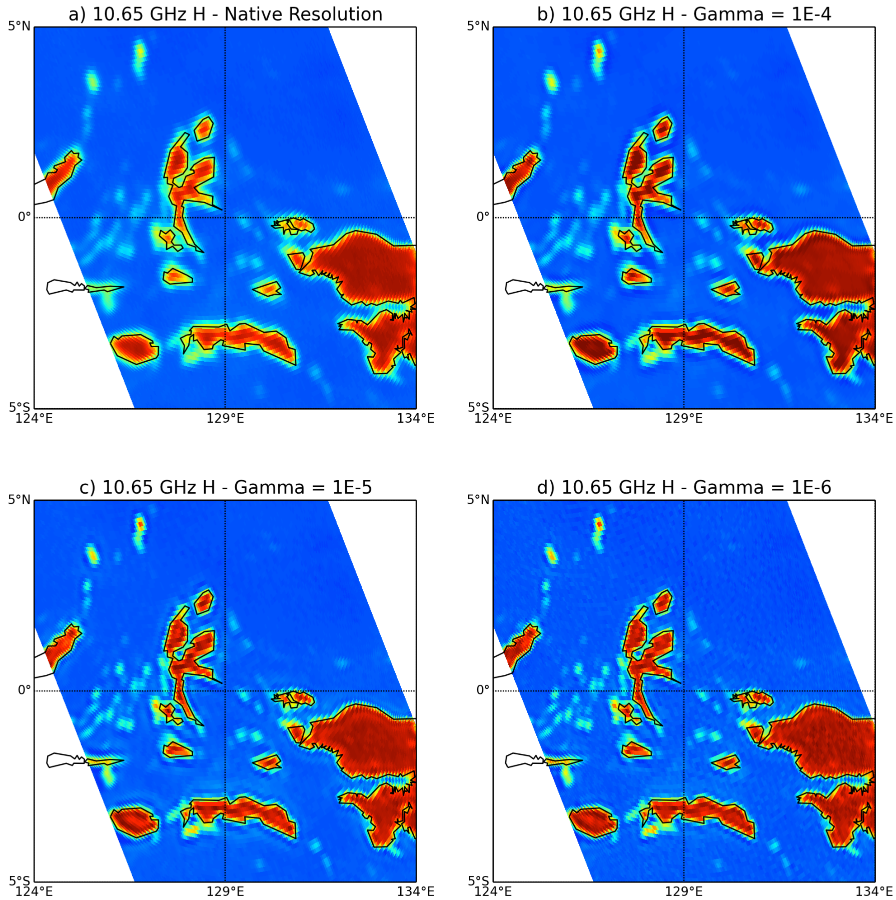

Figure 6. The effect of variations of the tuning parameter γ on the deconvolution of the 10.65 GHz channels, as applied to real data. a) Native resolution. b) $\gamma = 1.0 \times 10^{-4}$ c) $\gamma = 1.0 \times 10^{-5}$ d) $\gamma = 1.0 \times 10^{-6}$

Atmos. Meas. Tech. Discuss., doi:10.5194/amt-2016-275, 2016
Manuscript under review for journal Atmos. Meas. Tech.
Published: 31 August 2016

Atmospheric Measurement Techniques
Discussions
Open Access

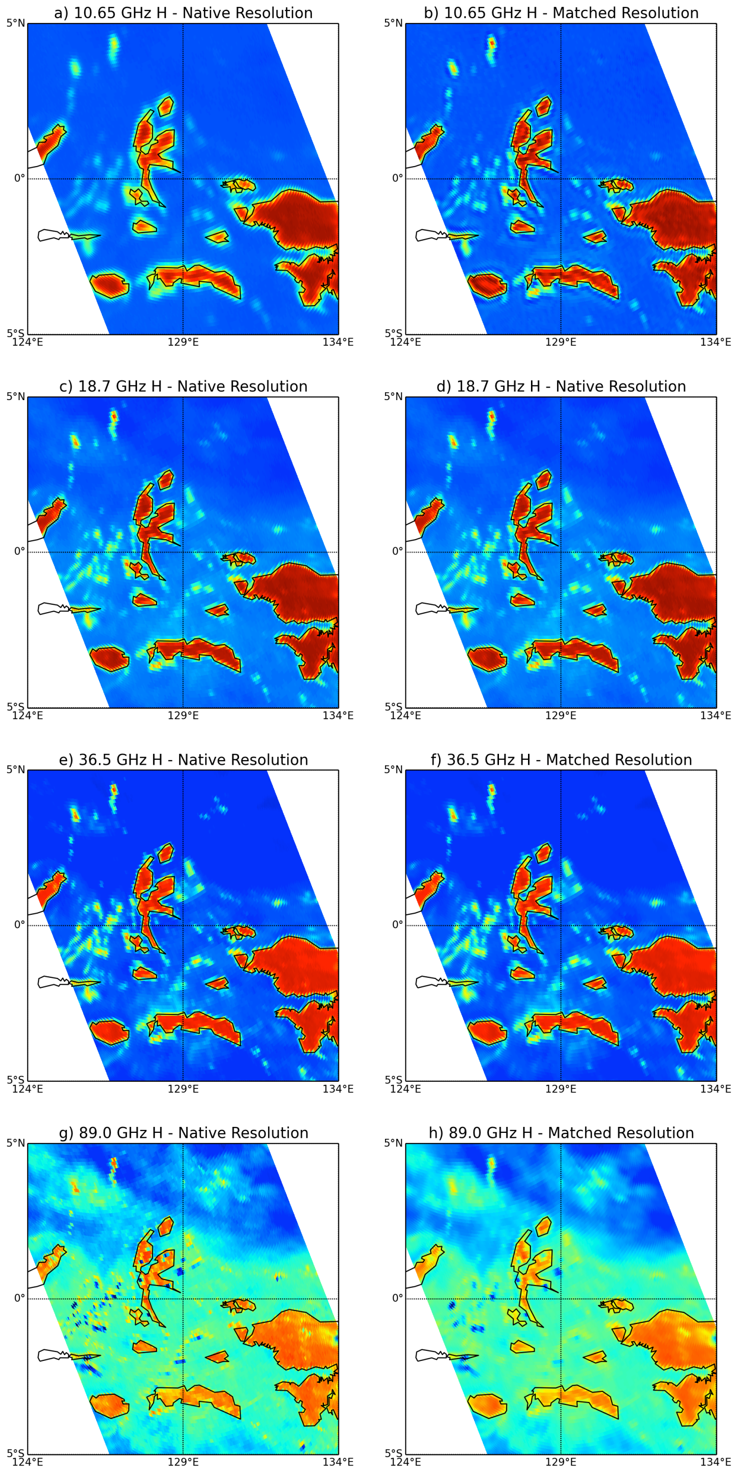

Figure 7. A sample of GMI imagery before (left column) and after (right column) the resolution matching procedure. For 18.70 GHz, which defines the target EFOV, no adjustment is made.

Atmos. Meas. Tech. Discuss., doi:10.5194/amt-2016-275, 2016
Manuscript under review for journal Atmos. Meas. Tech.
Published: 31 August 2016

Table 1. Instantaneous and effective fields-of-view (native) for GMI channels. Channels are identified by their frequency in GHz and their polarization (V = vertical, H = horizontal).

	3 dB Beamwidth [km]		
Channel	**Cross-scan**	**Along-scan (IFOV)**	**Along-scan (EFOV)**
10.65 V,H	32.1	19.4	19.8
18.70 V,H	18.1	10.9	11.7
23.80 V	16.0	9.7	10.5
36.50 V,H	15.6	9.4	10.3
89.00 V,H	7.2	4.4	6.4
166.00 V,H	6.3	4.1	5.8
183.31 $\pm$ 3 V	5.8	3.8	5.6
183.31 $\pm$ 7 V	5.8	3.8	5.6

Atmos. Meas. Tech. Discuss., doi:10.5194/amt-2016-275, 2016
Manuscript under review for journal Atmos. Meas. Tech.
Published: 31 August 2016

Atmospheric Measurement Techniques Discussions
Open Access

Table 2. Measured and inferred satellite/sensor characteristics determined from actual GMI data so as construct a self-consistent geometric scan model. These values should be consider typical rather than absolute.

Parameter		**Value**
Altitude		407.16 km
GMI geographic coverage (low freq.)		to $\pm 69.4^\circ$ latitude
Orbital period		5554 sec
Scans per orbit		2963 sec
Scan direction		Counterclockwise
Scan period		1.874 sec
Scan range		152.6°
Pixels per scan		221
Integration time		3.594 msec
Along-track scan separation		13.15 km
Scan displacement between low and high frequencies		4.1 ± 0.1 scans
Scan radius (great circle)	Low freq.	480.7 km
	High freq.	426.0 km
Swath width	Low freq.	931.2 km
	High freq.	825.4 km
Along-scan pixel separation	Low freq.	5.787 km
	High freq.	5.130 km
Earth incidence angle	Low freq.	52.78° km
	High freq.	49.11°

Table 3. Comparison of native and resolution-matched EFOV 3 dB widths [km].

Frequency	**Cross-scan**		**Along-scan**	
	Native	**Matched**	**Native**	**Matched**
10.65	32.1	26.5	19.8	16.5
18.70	18.1	18.1	11.8	11.8
23.80	16.0	18.0	10.6	11.8
36.50	15.6	18.0	10.3	11.8
89.00	7.2	—	6.3	11.8